Impact of metal/ceramic interactions on interfacial shear strength: Study of Cr/TiN using a new modified embedded-atom potential

Nisha Dhariwal [a], Abu Shama Mohammad Miraz [a], W.J. Meng [b], Bala R. Ramachandran [c], Collin D. Wick [a],*

[a] College of Engineering & Science, Louisiana Tech University, Ruston, LA 71272, USA
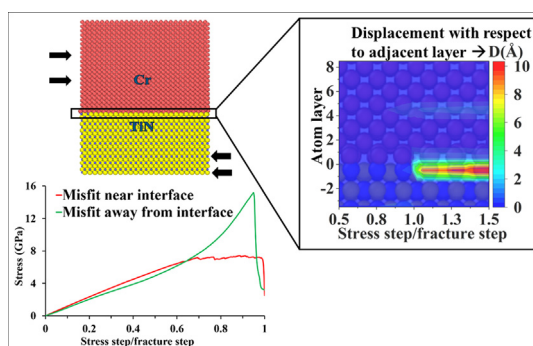[b] Department of Mechanical & Industrial Engineering, Louisiana State University, Baton Rouge, LA 70803, USA
[c] Institute for Micromanufacturing, Louisiana Tech University, Ruston, LA 71272, USA

HIGHLIGHTS

- Modified embedded atom method interatomic potential model for Cr/TiN.
- Generalized stacking fault energy is directly related to shear strength.
- The maximum shear stress of 7.2 GPa was observed Cr/TiN.
- Stronger interactions and better lattice matching led to higher shear strength.
- Cr metal is stronger than Cu and Ti with nitrides, in agreement with experiment.

GRAPHICAL ABSTRACT

ARTICLE INFO

ABSTRACT

The effect of misfit dislocation networks (MDNs) on the stability and shear strength of Cr/TiN was investigated using a newly developed modified embedded atom model parameterized to pure Cr, CrTi, CrN, and Cr/TiN interfacial properties. The interfacial energy was lowest when the MDN was located in the Cr layer adjacent to the chemical interface, which also had the largest dislocation core widths. This was consistent with generalized stacking fault energies, which had lower energy barriers between the first and second Cr layers next to the chemical interface. As the MDN moved away from the interface, dislocation core widths consistently decreased along with the interfacial energy. For all positions of MDNs, shear failure occurred in the ceramic, between the first and second TiN layers next to the chemical interface. The lowest shear strength was found for the system with the MDN in the first Cr layer with respect to the chemical interface. Only for this particular configuration was there a significant plastic deformation present.

1. Introduction

Metal/ceramic systems have numerous applications in areas such as structural composites, electronic devices, thermal barrier coatings on gas and jet turbine engines, high-temperature aircraft structures, wear-resistant materials, and medical implants [1–8]. Their overall performance depends on the properties of their interfaces [9], and interfacial failures can limit their durability [10]. Transition metal nitrides such as TiN and CrN are good candidates for coatings on machining tools due to their high hardness, high melting point, and good wear resistance [11–17]. However, they may display low adhesion to the substrate in many cases [14]. An improved interfacial mechanical integrity can often be achieved

---

* Corresponding author.
  E-mail address: cwick@latech.edu (C.D. Wick).

by the addition of thin metal interlayers between the ceramic coating and the substrate [18]. A detailed understanding of the structure and mechanical behavior of metal/ceramic interfaces will facilitate the selection of materials for stable metal/ceramic systems with desired strength [19]. This can be achieved by combining experimental methods with multiscale modeling and simulation techniques [20–22], providing atomic-level insights that are verified by experimental measurements.

The strength of the metal/ceramic systems against external shear is an important property from the material design perspective. Experimental techniques, such as axial compression loading of micropillar specimens containing metal/ceramic interfacial regions, fabricated with focused ion beam micro/nano scale machining, and *in-situ* indentation in a transmission electron microscope, have been utilized in producing quantitative data, such as the average critical shear stress, for the mechanical failure of metal/ceramic interfaces [23–26]. Specifically, research on multilayered Al/TiN showed enhanced plastic co-deformation [27] at the individual layer thickness of 5 nm or below during indentation studies. The mechanical properties of Al/SiC films were studied under shear loading and the dependence of the failure behavior on layer thickness was observed [28]. Such unique properties provided a potential of designing novel metal/ceramic composites with enhanced hardness and ductility. A recent experimental study provided details on the mechanical failure of Cr/CrN [29], Cu/CrN and Ti/CrN interfaces under shear loading [23]. It was established that the critical shear stress of the coating/substrate system depended on the metal interlayer used. As compared to Cu and Ti, Cr interlayer displayed highest critical shear stress for failure. The addition of a Cr metal interlayer between CrN (or TiN) and the underlying substrates, such as stainless steel or Ti6Al4V alloys [14,30,31] has been shown to improve their strength and stability by reducing the stress between the ceramic and the substrate. Additionally, the presence of Cr interlayers has been found to improve the corrosion and wear resistance [32–35], and the high-temperature oxidation resistance of different alloys [36,37]. However, the interfacial behavior of chromium interlayer-based metal/ceramic systems at the atomic level is still unclear.

Atomic level simulations can provide a detailed understanding of the factors that contribute to interfacial strength and stability. First-principles density functional theory (DFT) is an attractive choice due to its flexibility in studying a large array of systems without the need for parameterizing atomic models. Many DFT studies focus on the investigation of work of adhesion (WoA) of metal/ceramic interfaces [38–40], interface-driven twinning [41], phase transitions [42,43] and tensile or shear strength of the interface [44,45]. Recent DFT calculations found that resistance to shear was highest for Cr/TiN in comparison to many metal/ceramic combinations [46]. This was attributed to Cr/TiN having the highest overall generalized stacking fault energy (GSFE) barrier near the interface of the systems studied [46]. Validating this requires expanding the simulations to larger scales to directly calculate the shear strength of Cr/TiN. However, due to the higher computational costs, *ab initio* DFT techniques are infeasible for the study of large systems.

To understand the structure-property relationships of Cr/TiN metal/ceramic systems through large scale simulations, reliably parameterized interaction potentials are needed. The modified embedded atom method (MEAM) developed by Baskes *et al.* [47] has been widely used for many metals including fcc, bcc, and hcp [48–56], along with different ceramics, such as TiN and CrN [13,57,58]. Simulations with the MEAM model have also been shown to scale to very large system sizes [59–61]. Metal/ceramic interfaces have recently been examined with MEAM potentials,

providing information on their interfacial stability, the influence of misfit dislocations (MDNs), and shear strength [62–64].

Based on the above consideration and building upon the previous work related to the study of the effect of MDNs on the mechanical response of Ti/TiN and Cu/TiN interfaces [62], the present work is aimed at developing a new interatomic potential for the interaction of Cr with TiN and studying their interfacial behavior. While a considerable amount of work has been done on the study of fcc metal/TiN [44,45,65] and hcp metal/TiN interfaces [14,62,66,67], to the author's knowledge, no previous work has studied the interfacial behavior of bcc metal/NaCl-type TiN interfaces. This paper represents the development of a new Cr/TiN MEAM model, and the investigation into the role of the presence and location of MDNs on its shear strength. From previous computational work, it is anticipated the Cr will have stronger interactions with TiN than fcc and hcp metals [46], and experimentally, Cr has higher shear strength with CrN than Ti or Cu [23]. The parametrization and simulation methodology developed will help bring *ab initio* predictions closer to experimentally measured results, to further validate their abilities for use in materials design.

2. Methodology

2.1. Interatomic Potential: MEAM formalism

The details of the MEAM formalism have been reported in the literature [47]. In brief, the total energy of a system is the sum of an embedding function, F_i, and a pair interaction, $\varphi_{ij}(R_{ij})$ between atoms i and j separated by a distance R_{ij},

$$E\text{total} = \sum_i \left[F_i(\bar{\rho}_i) + \frac{1}{2} \sum_{j \neq i} S_{ij} \varphi_{ij}(R_{ij}) \right] \tag{1}$$

$$F(\bar{\rho}) = AE_c \left(\bar{\rho} / \bar{\rho}^0 \right) ln \left(\bar{\rho} / \bar{\rho}^0 \right) \tag{2}$$

where A is an adjustable parameter, E_c is the cohesive energy, and $\bar{\rho}^0$ is the background electron density for a reference structure. $\bar{\rho}$ is the background electron density at the atomic site i that can be computed by combining the partial electron density terms for different angular contributions [53]. Several expressions for combining the partial electron densities have been proposed [68]. Among them, the following form has been widely used:

$$\bar{\rho}_i = \rho_i^{(0)} G(\Gamma) \tag{3}$$

where

$$G(\Gamma) = 2/(1 + e^{-\Gamma}) \tag{4}$$

and

$$\Gamma = \sum_{h=1}^{3} t_i^{(h)} \left[\rho_i^{(h)} / \rho_i^{(0)} \right]^2 \tag{5}$$

$t_i^{(h)}$ are the weight factors. The atomic electron density is given as

$$\rho_j^{(h)}(R) = \rho_0 e^{-\beta^{(h)} \left(\frac{R}{r_e} - 1 \right)} \tag{6}$$

which involves the adjustable parameters $\beta^{(0)}$, $\beta^{(1)}$, $\beta^{(2)}$, $\beta^{(3)}$ and r_e, the nearest neighbor distance in the equilibrium reference structure. The total energy per atom for a given reference structure is evaluated from the universal equation of state by Rose *et al.* [69] as a function of nearest neighbor distance R,

$$F\left[\bar{\rho}^0(R) \right] + \frac{1}{2} \sum \phi(R) = E^u(R) = -E_c(1 + a^*)e^{-a^*} \tag{7}$$

where

$$a^* = \alpha\left(\frac{R}{r_e} - 1\right) \qquad (8)$$

α is an adjustable parameter that includes contributions from the bulk modulus, cohesive energy, and equilibrium atomic volume. S_{ij}, as given in Eq. (1), is a three-body screening factor that denotes the effect of the position of a third atom, k, on the interaction between atoms i and j, which is limited by C_{min} (S_{ij} = 0) and C_{max} (S_{ij} = 1) as described in detail in the literature [70].

2.2. Determination of MEAM parameters

For a single element, once the reference structure is defined, including its E_c and r_e, which are set to experiment, 11 remaining MEAM parameters need to be determined: $\beta^{(0)}$, $\beta^{(1)}$, $\beta^{(2)}$, $\beta^{(3)}$, $t^{(1)}$, $t^{(2)}$, $t^{(3)}$, A, α, C_{min}, and C_{max}. The values for the MEAM parameters for N were taken from the literature without any modification [58]. The reference structures for Ti and Cr are hcp and bcc, respectively. This requires fitting eleven additional parameters for the binary systems. These include the E_c between them in Eq. (2), along with their α and r_e values in Eq. (8). The remaining eight parameters are their C_{min} and C_{max} values. For ternary interactions, an additional six parameters, three C_{min} and three C_{max}, need to be fit. For Ti and TiN, the previously developed model designed to study the Ti/TiN interface was used [62]. A model for pure Cr was parameterized (Table 1), along with a model for CrN, Cr$_2$Ti [71,72] (Table 3) and the Cr/TiN interface (Table 4). A model for CrN was recently developed by Ding et al [13], while no model for the CrTi binary system is currently available to the best of the knowledge of the authors.

An in-house Python code developed by this research group [73] was used for the optimization of a set of MEAM parameters by minimizing the mean square displacement between the calculated and experimental/DFT derived properties. The method uses a combination of minimization and a genetic algorithm.

2.3. Computational details

2.3.1. DFT calculations

The properties were extracted from a combination of experimental measurements and DFT calculations. Most of the DFT calculations were carried out for this work, even if values existed in the literature. The Vienna ab initio simulation package [74] was utilized for the DFT calculations using the Perdew, Burke, and Ernzerhof generalized gradient approximation for the exchange-correlation functional [75,76]. The potential due to the core electrons was accounted for by the projector augmented wave method [77], which combined the features of the pseudopotential approach and the linear augmented plane wave method. Kohn-Sham orbitals for valence electrons were expanded in terms of a plane wave basis set with a cutoff energy of 400 eV. The Monkhorst-Pack scheme was used for sampling the k-point of the plane wave basis in the first Brillouin zone [78]. The specific k-point mesh size depended on the system size and the calculation being carried out. For pure Cr, the monovacancy formation energy,

Table 2
Comparison of the DFT calculated/experimental properties of Cr with values obtained from the MEAM model.

Property	DFT/expt. value	New model	Lee model [88]
E_{vac} (eV)	2.57[a], 2.27[b]	3.17	1.95
E_s (0 0 1) (J/m^2)	2.50[a]	2.85	2.39
E_s (1 1 0) (J/m^2)	2.34[a], 2.35[c]	2.69	2.26
E_s (1 1 1) (J/m^2)	2.60[a]	3.07	2.44
Elastic constants (GPa)			
C_{11}	391.0[d]	455.91	344.40
C_{12}	89.60[d]	69.76	112.80
C_{44}	103.20[d]	112.11	130.40
ρ_s (g/cm^3)	7.15[e]	7.28	7.25
E_{fcc}/E_{bcc}	0.96[a]	0.92	0.97
E_{hcp}/E_{bcc}	0.95[a]	0.93	0.98

[a] DFT as calculated in this work.
[b] Reference [89].
[c] Reference [90].
[d] Reference [91].
[e] Reference [92].

Table 3
MEAM potential parameters for the binary systems (x-y). In any pair, the first element is denoted by x, and the second element is denoted by y.

Parameters	(x-y) pair		
	Cr-N	Cr-Ti	Ti-N [62]
Reference state	b1	b1	b1
E_c (x, y) (eV)	5.5269	2.9859	6.6139
r_e (x, y) (Å)	2.1069	2.6952	2.1195
α (x, y)	6.9415	7.3082	4.7225
C_{min} (x, x, y)	0.08	2.0	0.4263
C_{min} (y, y, x)	1.4265	1.88	1.0733
C_{min} (x, y, x)	1.7054	0.22	1.5
C_{min} (x, y, y)	1.75	1.2036	1.5
C_{max} (x, x, y)	2.18	3.4196	2.0328
C_{max} (y, y, x)	3.814	3.2941	1.7998
C_{max} (x, y, x)	2.891	2.0	2.4073
C_{max} (x, y, y)	4.0	2.198	2.3557

Table 4
MEAM potential parameters for the Cr/TiN ternary system.

Parameters	Value
C_{min} (Cr, N, Ti)	1.9376
C_{min} (Cr, Ti, N)	0.9440
C_{min} (N, Ti, Cr)	0.7918
C_{max} (Cr, N, Ti)	3.8510
C_{max} (Cr, Ti, N)	3.6540
C_{max} (N, Ti, Cr)	3.1064

surface energies, and the GSFEs were calculated using first-principles DFT. In order to calculate the monovacancy formation energy, the Brillouin zone was sampled using 3 × 3 × 3 mesh of k-points for the 128-atom cells. The surface energies were calculated for the surfaces Cr(0 0 1), Cr(1 1 0), and Cr(1 1 1) with the system sizes of 54, 72, and 48 atoms respectively and the Brillouin zone was sampled using 4 × 4 × 1 k-point mesh. For each of these

Table 1
MEAM potential parameter sets for pure Cr, Ti, and N.

	E_c (eV)	r_e (Å)	A	α	$\beta^{(0)}$	$\beta^{(1)}$	$\beta^{(2)}$	$\beta^{(3)}$	$t^{(1)}$	$t^{(2)}$	$t^{(3)}$	C_{min}	C_{max}
Cr	4.10[a]	2.88[b]	0.28	5.70	8.74	0.01	5.48	0.37	1.06	11.09	−7.73	0.75	2.36
Ti	4.87	2.92	1.19	4.41	1.58	0.08	2.89	0.0016	5.55	6.79	−2.05	0.89	2.85
N	4.88	1.10	1.80	5.96	2.75	4.00	4.00	4.00	0.05	1.00	0.00	2.00	2.80

[a] Reference [87].
[b] Reference [86].

surfaces, a periodic system with 15 Å of vacuum was created, resulting in the formation of two surfaces with the specified orientations.

The GSFE surface was calculated for the Cr(001) system. For this calculation, half of the atoms were displaced in the X[110] and Y[$\bar{1}$10] directions, keeping the other half of atoms fixed, as had been done previously [46]. A total of ten positions along X and ten along the Y directions were sampled, mapping a total of 100 points. For each point, an energy minimization followed their displacement, allowing the atoms to only relax in the Z direction (keeping X and Y positions all fixed). The minimum energy path was then plotted along the X direction after mapping the full GSFEs out [79]. The maximum height of the minimum energy plot along the X direction defines the energy barrier of the shear displacement of the GSFE surfaces.

For the binary systems, the elastic constants, surface energies, and the enthalpies of mixing were calculated using DFT. The elastic constants were calculated using a system size of 64 atoms for CrN and 24 atoms for Cr_2Ti with a $12 \times 12 \times 12$ k-point mesh. To calculate the enthalpy of mixing, a Cr_2Ti system of 24 atoms and a CrN system of 32 atoms were used, each with a $4 \times 4 \times 4$ k-point mesh. For the surface energy calculations, 72, 32 and 54 atoms were used for CrN(001), CrN(110) and CrN(111) while 48, 44 and 72 atoms were used for Cr_2Ti(001), Cr_2Ti(110) and Cr_2Ti(111). In each of these systems, 15 Å of vacuum was present normal to the surface in consideration, and a k-point grid of $4 \times 4 \times 1$ was used for the surface calculations. The impact of spin-polarized calculations was investigated for all the systems, and it was found that they only had a significant impact on the structure and energetics of CrN, so only the CrN properties include spin polarization.

For Cr/TiN interfaces, the WoA was calculated for a system that consisted of eight layers of four Cr atoms (32 total) along with six layers of eight TiN atoms (48 total) that formed a single interface between Cr(001) and TiN(001). The interface was perpendicular to the Z-direction in a cell of approximate dimensions of $5.88 \times 5.88 \times 40$ Å. As with the previous work [46], there was at least 10 Å of vacuum present along the Z direction to assure that only one interface was formed in between Cr and TiN. The WoA for the Cr/TiN interface was calculated as done previously [80]:

$$WoA = (E_{Cr} + E_{TiN} - E_{Cr/TiN})/A \tag{9}$$

where $E_{Cr/TiN}$ is the energy of the entire system, and E_{Cr} is the energy of the Cr(001) system optimized in both atomic positions and cell coordinates. E_{TiN} is the energy of an optimized TiN(001) system, and A is the area of the Cr/TiN interface.

For the GSFE surface of the Cr/TiN system, the configuration was the same as for the WoA, and it was calculated at the chemical interface between the Cr(001) and the TiN(001) surfaces. This was denoted as P = 0 (see Fig. 1(a)). The GSFE surface was also calculated for the P = 1 layer, which was in between the TiN(001) surface with one Cr(001) layer (4 additional atoms) and the remaining eleven Cr(001) layers (44 atoms). The GSFE surface for Cr/TiN was mapped out using the procedure described above, i.e., by displacing all the atoms above the planes P = 0 or P = 1 from one lattice point to another equivalent lattice point along the X [110] and Y[$\bar{1}$10] directions (Fig. 1(b)), keeping the positions of all the atoms below those planes fixed, followed by relaxation along the Z direction.

2.3.2. Calculation of properties from the MEAM model

All the MEAM properties were calculated using the LAMMPS simulation software [81]. For Cr, the lattice parameters, ratios of the energy of different crystal structures (E_{fcc}/E_{bcc}) and (E_{hcp}/E_{bcc}), surface energies (E_s) of various surfaces Cr(001), Cr(110), Cr(111), solid density (ρ_s), elastic constants, and monovacancy formation energy (E_{vac}) were calculated [73]. For all calculations except the solid density, energy minimizations were carried out with the conjugate gradient method. The fcc system had 32 atoms, the hcp system had 48 atoms, and the bcc system had 54 atoms. To calculate the monovacancy formation energy for Cr, one atom was removed from the bcc system of 128 atoms. The elastic constant calculations were carried out for the bcc system with 54 atoms, and systems with 54, 72, and 48 atoms were used for the calculation of surface energies of Cr(001), Cr(110), and Cr(111) surfaces, respectively. To calculate the solid density for Cr metal, 20 ps of NPT simulations of a system with 432 atoms were carried out at 298 K and 1 atm using the Nosè-Hoover thermostat and barostat [82,83] with a timestep of 1 fs.
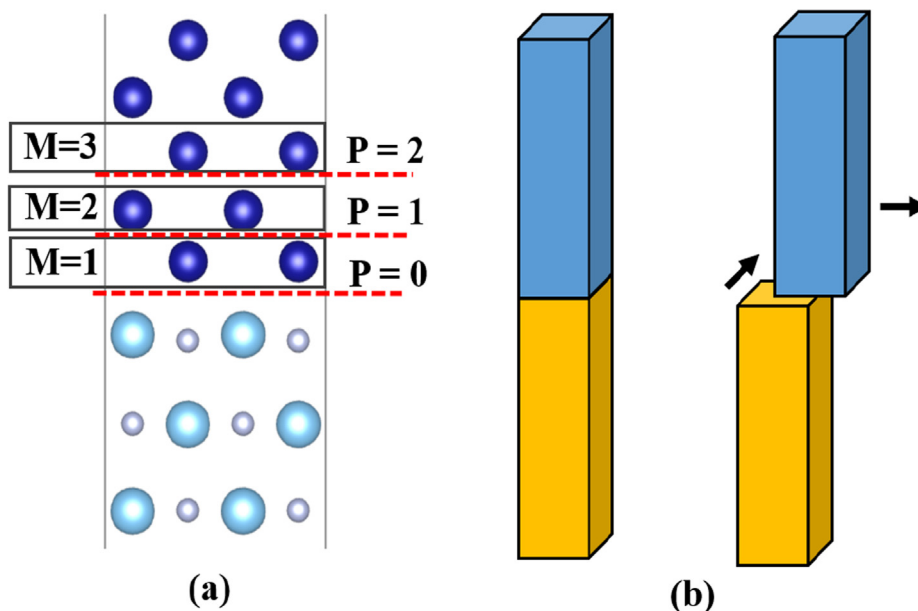

Fig. 1. (a) Cr(001)/TiN(001) structure with the atomic layers denoted by M and the interlayer planes denoted by P, (b) Schematic of the shear displacements for calculating the GSFE surface of the Cr/TiN metal/ceramic system.

For binary systems, the enthalpy of mixing and WoA were calculated for CrN and Cr_2Ti. The enthalpy of mixing was calculated using a system of 192 atoms for CrN, and a system of 216 atoms for Cr_2Ti. The surface energies were calculated using a system size of 108 atoms for CrN(001), 144 atoms for both CrN(110) and CrN (111) surfaces, 48 atoms for Cr_2Ti (001), 44 atoms for Cr_2Ti (110), and 72 atoms for the Cr_2Ti (111) surface. The elastic constants, GSFE, and WoA were calculated using the same system sizes as used in DFT calculations described in Section 2.3.1.

2.3.3. Large scale MD simulations

The Baker-Nutting orientation relationship [84]—with $[100]_{NaCl}$ || $[110]_{bcc}$ along the X axis, $[010]_{NaCl}$ || $[\bar{1}10]_{bcc}$ along the Y axis, and $(001)_{NaCl}$ || $(001)_{bcc}$ along the Z axis—was adopted between the rock salt (B1) structured TiN and bcc Cr (Fig. 2). The interface was parallel to the X-Y plane, with each dimension close to 7.5 nm in the initial structures. The total thickness in the Z direction was approximately 10 nm, with 6 nm of Cr and 4 nm of TiN present. The plane separating Cr and TiN phases was defined as the chemical interface. The first Cr layer next to this interface was denoted by M = 1, the second layer by M = 2, and so on (see Fig. 1(a)). The equilibrium interfacial structure was obtained by an initial relaxation followed by an iterative conjugate-gradient stress-relief treatment [85]. The preliminary relaxation was carried out through an NVT equilibration at 10 K for 50 ps in which the top and the bottom two layers in the Z direction were fixed. The iterative stress-relief treatment was conducted to adjust the magnitude of the normal stress components to be less than 100 Pa.

The relaxed structure was then subjected to a quasi-static, stress-controlled shear loading parallel to the interfacial plane with a stress step size of 50 MPa. Controlled shear stresses were applied in equal amounts on both the Cr and TiN layers using an incremental deformation gradient computed from the elastic constants of Cr and TiN [85]. The system was allowed to equilibrate in each step by first running a 1 ps NVT equilibration at 5 K, followed by a conjugate-gradient relaxation.
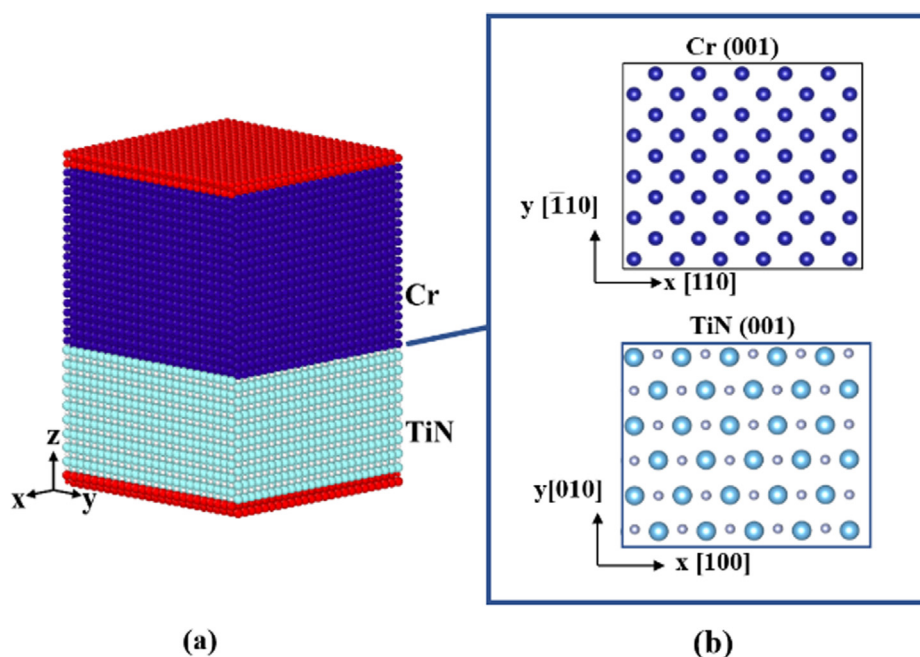
3. Results and discussion

3.1. Pure Cr metal

Table 1 shows the newly determined MEAM parameter values for Cr, along with the MEAM parameter values used for this work for Ti [62] and N [58] taken from the literature. The values for E_c and r_e for Cr were taken from the experimental values in the literature [86,87]. The experimental/DFT and the MEAM calculated values of the various properties of Cr using the present model, as well as Lee's model [88], are listed in Table 2.

As can be observed from Table 2, reasonable agreement with experimental/DFT values was achieved with both MEAM models. In particular, the bcc structure was the most stable, and the correct order among the low index surface energies was achieved for both models. While good agreement with the properties outlined in Table 2 were sought, the focus of this work was to model interfacial shear resistance. The GSFE surfaces are relevant to the dislocation movement under shear stress which impact the overall resistance of surfaces to shear [85], which is why it was also used in the parameterization of the new MEAM model.

Fig. 3(a-c) show the GSFE surfaces of Cr(001) calculated by DFT, the new MEAM model, and the model by Lee et al. [88]. The new model did a good job of reproducing the GSFE from DFT, while having a slightly different shape than the DFT calculations. The Lee model underestimated the GSFE barriers to a moderate degree. The minimum energy path on these GSFEs plotted as a function of position along the X axis is shown in Fig. 3(d). For this system, the path ended up as simply the energy at Y = 0 as a function of X since the minimum energy path is parallel to the X axis. The new model, again, reproduced the DFT barrier height in the minimum energy pathway with good accuracy, while the Lee model underestimated it by around 30%. The GSFE for Cr(110) surface was also calculated and is provided in the Supplementary Information (Fig. S1), showing reasonable agreement with DFT results, underestimating the barrier by about 20%.

Fig. 2. (a) Cr(001)/TiN(001) structure (b) orientation relationship in Cr/TiN multilayers. The top and the bottom red colored regions are the fixed atoms. (For interpretation of the references to color in this figure legend, the reader is referred to the web version of this article.)
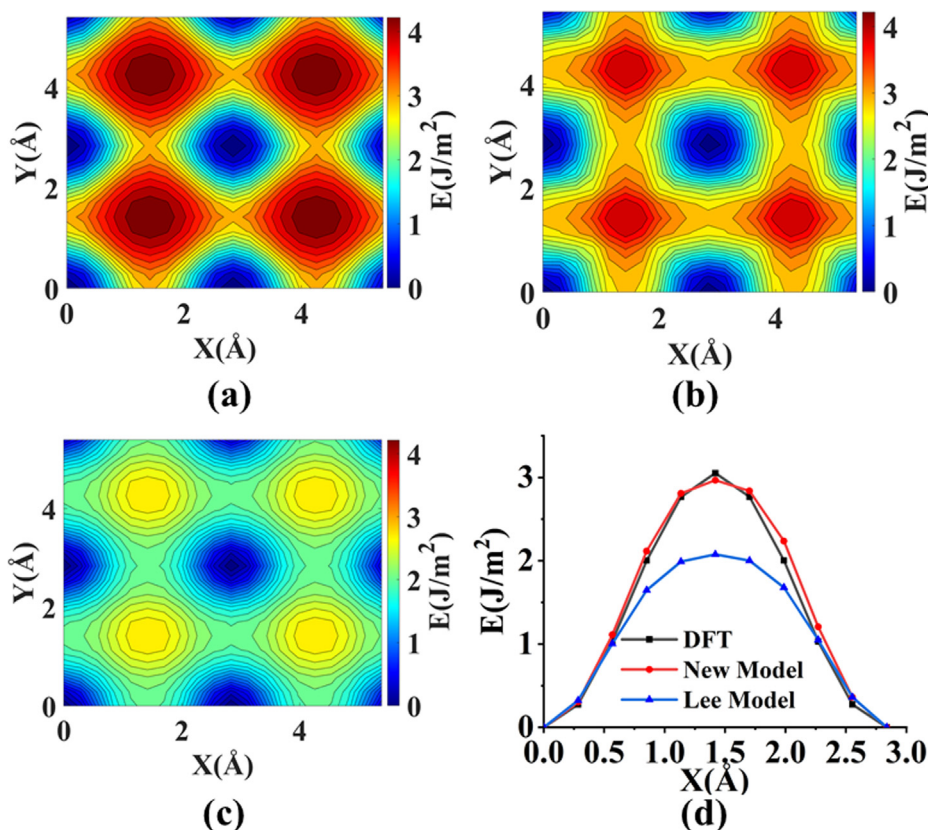
Fig. 3. GSFEs of Cr(001) calculated using (a) DFT, (b) new model (c) Lee model [88] (d) Comparison of minimum energy path of the GSFE for Cr(001).

3.2. Mixed systems

The binary parameters for Cr-Ti and Cr-N were fit to several properties, including enthalpies of mixing, elastic constants, and surface energies. Table 3 shows the values of the binary parameters obtained in the present work and Ti-N binary parameters from previous work [62]. It should be noted that there are instances of $C_{max} > 2.8$ for the binary interactions. Previous work noted that for atomic mixtures, charge transfer can be significant [73]. This can be explicitly modeled with a charge transfer method [93,94], but at significantly increased computational cost. A larger C_{max} allows for longer ranged charge interactions to be implicitly modeled with the regular MEAM formalism and has been used previously to model mixtures [62,95].

The parameters for the ternary Cr/TiN system are shown in Table 4. The NaCl-type CrN and TiN (space group $Fm\bar{3}m$) were chosen as reference structures for the Cr-N and Ti-N binary systems. Since the Cr_2Ti (space group $Fd3m$) structure cannot be used as a reference for the MEAM packages in LAMMPS, an NaCl type CrTi reference structure was chosen. Despite choosing a different reference structure, the Cr-Ti interactions were parameterized to reproduce the enthalpy of mixing, elastic constants, and surface energies of Cr_2Ti.

The DFT and the MEAM calculated values of the various physical properties of CrN, Cr_2Ti, and the ternary Cr/TiN systems using the present model are presented in Table 5. The new model reproduced the target values to a reasonable extent. In particular, the enthalpies of mixing, elastic constants, and the order of stability of the different surfaces compared well for Cr_2Ti. A MEAM model for CrN was developed by Ding *et al.* [13] ("Ding model" in Table 5), which was parameterized to reproduce elastic constants extracted from CrN thin films [96] and DFT calculations without spin polarization. Because of this focus, the elastic constants calculated with

the Ding model were somewhat different in comparison with the new model, which focused on the Cr/TiN interfacial properties. While the surface energies of the new model had the same order as DFT, their magnitudes are consistently underestimated. The reason that a better agreement with the surface energies was not achieved is that improving CrN surface energies hindered the agreement with DFT for the WoA and GSFE surfaces of the Cr/TiN interface. Since the focus of this work was to model the Cr/TiN interface, a greater weight on the WoA and GSFEs was used than CrN surface energies in evaluating the new MEAM parameters.
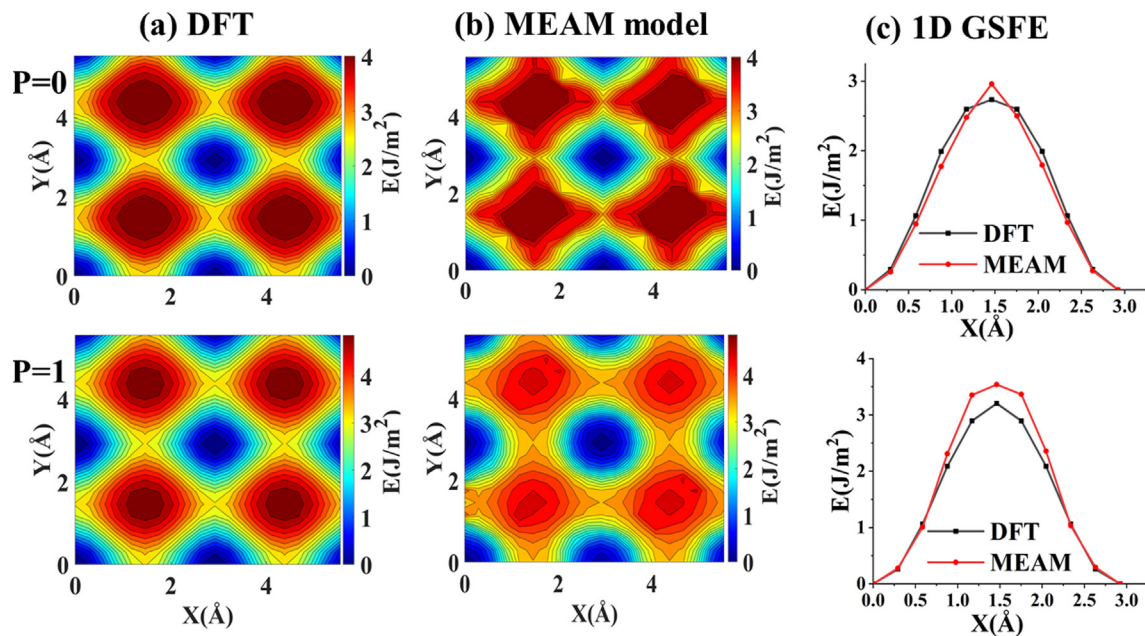
Fig. 4 shows a comparison of the GSFEs for the Cr(001)/TiN (001) interface for the P = 1 and P = 2 planes (see Fig. 1(a) for a description of P) calculated by the new model with the DFT results. While there were some subtle differences in the GSFE surfaces between DFT and the MEAM model, their overall agreement was good. Moreover, the minimum energy path and GSFE barrier heights had good agreement between DFT and the new MEAM model for both layers studied. For semi-coherent interfaces, smaller GSFE barriers have been shown to lead to larger dislocation core widths [46,99], which generally decrease shear strength [100,101]. Because of these reasons, reproducing GSFEs was one of the main focuses for the parameterization of the new MEAM model.

3.3. Stability of Cr/TiN systems

Large scale MD simulations were used to study the effect of the MDNs on the mechanical response of the Cr/TiN interfacial system under shear loading. MDNs were accommodated in successive metal layers and their relative energies were calculated to determine how MDN location influences interfacial stability and structure. MDNs were introduced by adding an extra row of atoms in both the X and Y direction in their respective layers. There were 25 atomic rows of TiN in the X and Y directions, and in a coherent

Table 5
Comparison of DFT calculated values of properties of binary CrN and Cr_2Ti and ternary Cr/TiN with the MEAM fitted values.

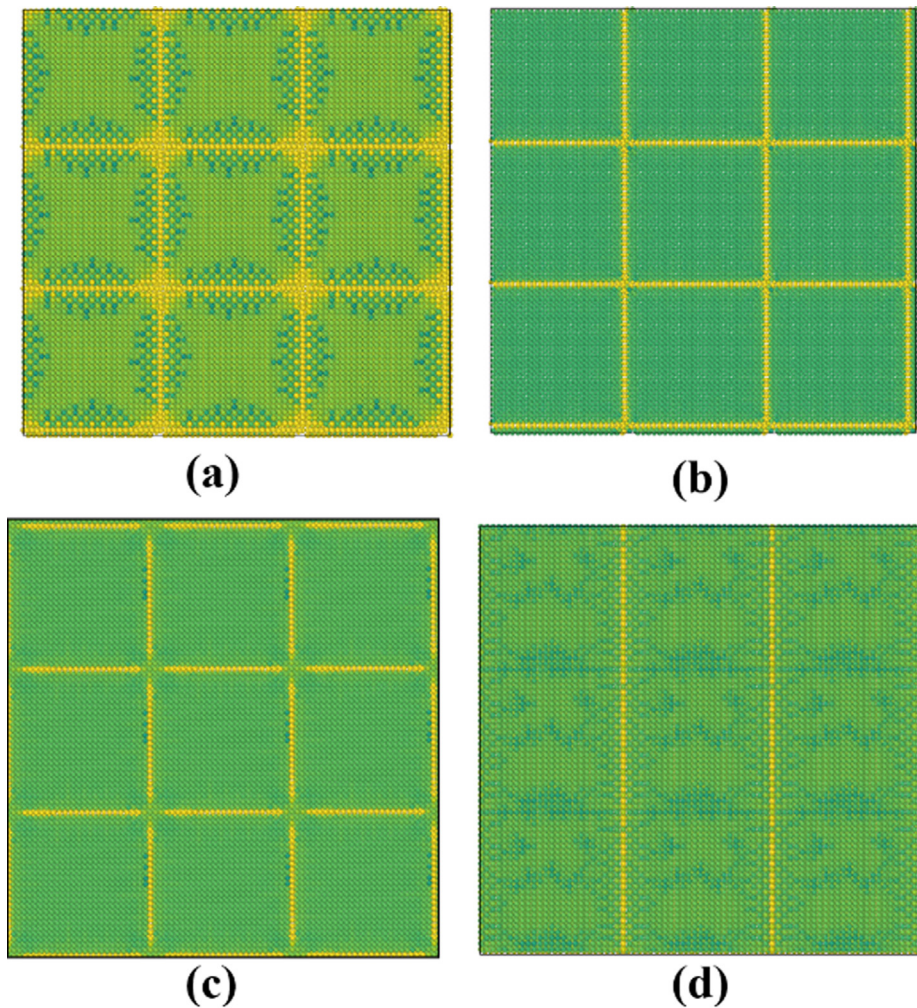| Property	System		DFT	MEAM	Ding Model[a]
Enthalpy of mixing ΔH_{mix} (eV/atom)	CrN		-1.65^b	-1.036	
	Cr_2Ti		$-0.11^{c,d}$	-0.109	
Elastic Constants (GPa)	CrN	C_{11}	319^c, 386^e	245	515
		C_{12}	117^c, 120^e	114	62
		C_{44}	60^c, 111^e	103	100
	Cr_2Ti	C_{11}	296^c, 287.3^f	251	
		C_{12}	154.3^c, 151.2^f	97	
		C_{44}	81.6^c, 81.1^f	58	
Surface energies E_S (J/m²)	CrN	CrN(001)	0.8088^c	0.3767	1.06
		CrN(110)	1.4602^c	0.7438	1.75
		CrN(111)	1.8264^c	1.0077	1.92
	Cr_2Ti	$Cr_2Ti(001)$	3.195^c	2.4220	
		$Cr_2Ti(110)$	1.436^c	1.5549	
		$Cr_2Ti(111)$	2.744^c	1.7224	
WoA (J/m²)	Cr/TiN		3.69^c	4.75	

[a] Reference [13].
[b] Reference [97].
[c] DFT calculated in this work.
[d] Reference [72].
[e] Reference [98].
[f] Reference [71].

Fig. 4. GSFEs of the Cr/TiN calculated using (a) DFT (b) MEAM for P = 0 and P = 1 planes. (c) A comparison of minimum energy path extracted from the GSFEs for P = 0 and P = 1.

interface between Cr and TiN, the same number of Cr atomic rows were present. For bulk TiN, the X dimension with 25 rows was 74.94 Å, while for bulk Cr, the X dimension was 72.02 Å. Hence, when adding an MDN, there were 26 rows of Cr, giving a bulk Cr X dimension of 74.91 Å, very close to equilibrium TiN. The proximity of each metal layer with respect to the chemical interface was denoted by the letter M, as shown in Fig. 1(a). When an MDN was located at a specific M layer, all Cr layers greater than or equal to M had additional Cr rows in the X and Y directions (except when noted otherwise), while those layers less than M (or in between the M layer and TiN) were coherent with the TiN interface. For instance, if the MDN was at the M = 1 layer, all Cr layers had additional rows, while for M = 4, the M = 1–3 layers did not have additional rows and were coherent with the TiN interface.

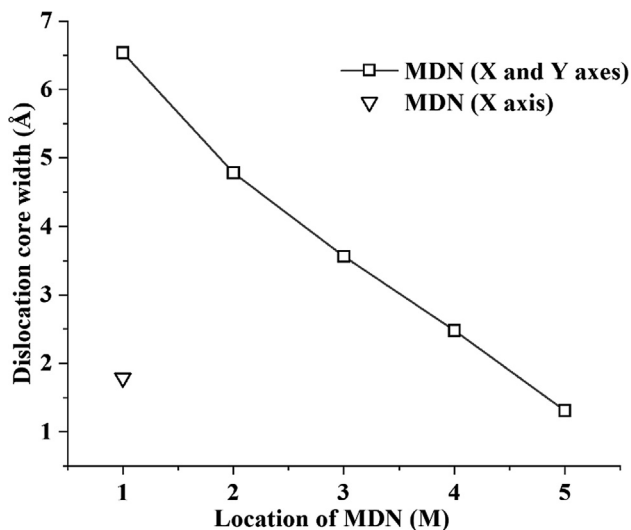The open software OVITO [102] was used for visualization and analysis. The centrosymmetric parameter (CSP), a measure of the lattice disorder around an atom, was used to characterize local atomic environment [103]. Fig. 5 shows atomic structures of the relaxed Cr/TiN interface with MDNs at the M = 1, M = 2, and M = 5 layers in both the X and Y directions. A system (Fig. 5(d)) with an MDN only in the X direction at M = 1 was also studied. To aid in viewing, the structures are replicated 3 times in the X and Y dimensions in the figures. The atoms are colored according to the CSP values with dark green atoms representing perfect lattice positions, yellow fully off-lattice, and light green in-between [103]. The layers shown are the one with the MDN (top), all layers between it and the ceramic, and the ceramic phase. The dislocation cores formed by the MDNs can easily be observed via the yellow bands present with the MDN at M = 1 having the largest core width. The network of edge-shaped misfit dislocation cores shown in Fig. 5(a-c) are similar to what was observed for other {001} stacking orientations, such as the Nb/NbC interface [84].

Fig. 5. MDN structure of Cr/TiN system at (a) M = 1, (b) M = 2, and (c) M = 5 (d) M = 1 (X axis only) layers. Atoms are color-coded according to CSP results.

Fig. 6 shows a plot of the dislocation core width for MDNs in different layers. The core widths were measured by calculating the width of the off-lattice regions as observed in Fig. 5 (atoms with a CSP > 20 [103]). The core widths of the dislocations gradually

Fig. 6. Dislocation core width with respect to the location of MDN (M).

decreased as the location of MDNs moves away from the interface. The intersection of the misfit dislocations results in the formation of nodes [84]. Fig. 5 shows that larger sized nodes are present for the system with MDNs at M = 1, and the node size decreases as the MDNs moves away from the interface with little to no node formation for the system with MDN at M = 5. The larger width of the dislocation cores for M = 1, which corresponds to semi-coherency at the P = 0 plane, is consistent with the fact that the GSFE for P = 0 has a lower amplitude than for P > 0 (see Fig. 4). An increase in GSFE barriers corresponds to reduced dislocation core widths, constricting the nodes at their intersection, which provide stronger pinning points to the motion of MDNs [85].

The interfacial energy (γ) of the Cr/TiN interface is calculated as follows:

$$\gamma = (E_{\text{interface}} - nE_{\text{Cr}} - mE_{\text{TiN}})/A \tag{10}$$

where $E_{\text{interface}}$ is the total potential energy of the bilayer system, A is the area of the interface, n is the number of Cr atoms, and m is the number of TiN groups. E_{Cr} and E_{TiN} are the cohesive energies of Cr and TiN, respectively. Fig. 7 gives the interfacial energy as a function of the location of the MDNs, where the energy of the fully coherent interface was subtracted from them for comparison.

The interfacial energy was found to be dependent on the location of the MDN and was lowest when the MDN was present at the interface due to the lower GSFE barriers at that layer (P = 0). There was a gradual increase in the interfacial free energy as the
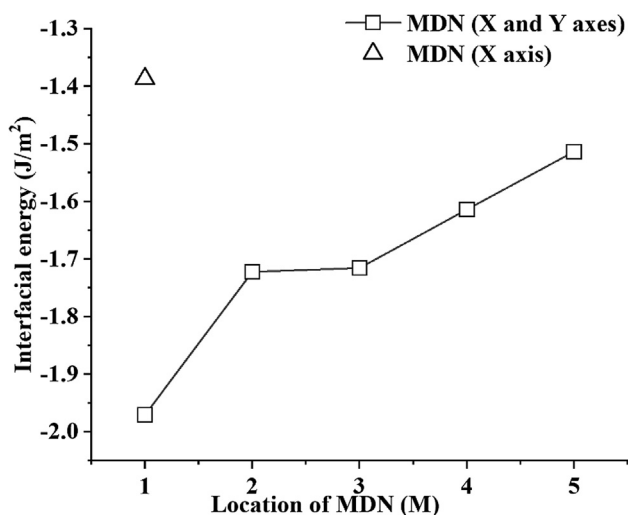
Fig. 7. Plot of the difference in the interfacial energy with respect to the coherent interfacial energy as a function of MDN location (M).

location of MDN moved further into the Cr layers. The increase in energy associated with larger M is due to the energy required to strain additional Cr layers to keep it coherent with the TiN surface. The interfacial energy for the configuration with the MDN at the M = 1 layer along one one axis is also shown in Fig. 7 and has a value that is significantly closer to the coherent energy than when the MDN is present in two axes at M = 1. This was expected as with the MDN in one direction, it more closely represents the higher energy coherent structure than with MDNs in two directions.

3.4. Impact of shear on Cr/TiN systems

The relaxed structure was subjected to a shear loading parallel to the interfacial plane in the X direction. Fig. 8 shows the variation in the shear strength of the interface as a function of the location of MDNs. All the structures with MDNs displayed a much lower yield strength than the coherent interface, which showed a maximum shear stress of 20 GPa. It can be seen from Fig. 8 that the maximum shear stress was lowest for the structure with the MDN at the interface (7.2 GPa) and gradually increases as the location of MDN moves away from the interface reaching 15.3 GPa for the MDN at M = 5. The shear response of the interface was observed to be related to the dislocation core width. The larger nodes in the M = 1 layer (corresponding to the lower GSFE barrier) causes
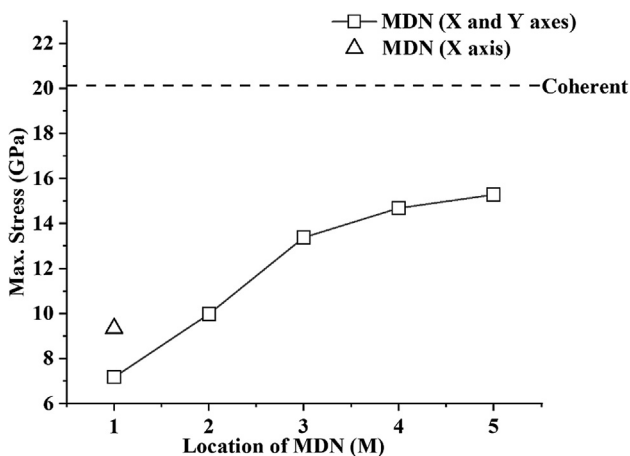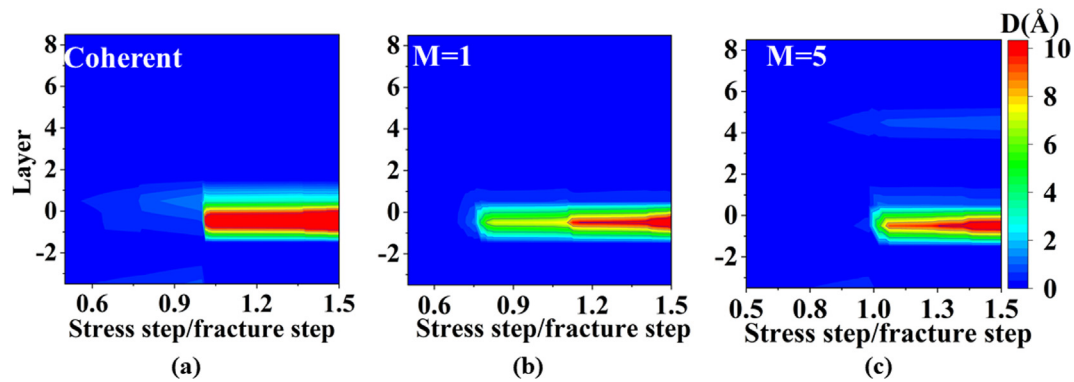

Fig. 8. Plot of interfacial shear strength vs. the location of MDN (M).

a reduced pinning force and therefore, reduces the shear strength of the interface. Additionally, Fig. 8 gives the shear strength when the MDN in the M = 1 layer was only in one direction perpendicular to the shear. It can be observed that the shear strength was moderately higher, 9.3 GPa vs. 7.2 GPa, with the MDN in one direction in comparison with it in both X and Y directions in the M = 1 layer. This is expected as the system with MDNs along two directions has much wider core sizes in comparison with the system with an MDN in one direction (see Fig. 6). Another aspect of the M = 1 system with MDNs in two directions, is that the nodes that are formed at the intersection of dislocation cores are significantly larger in size than the cores themselves, creating extended regions of local disorder (see Fig. 5(a)). For the M = 5 system, where the cores meet results in a node that is smaller in width than the cores themselves (see Fig. 5(c)). Overall, the larger regions of local disorder present in the M = 1 layer with MDNs in two directions reduces internal strain reducing its shear strength [85].
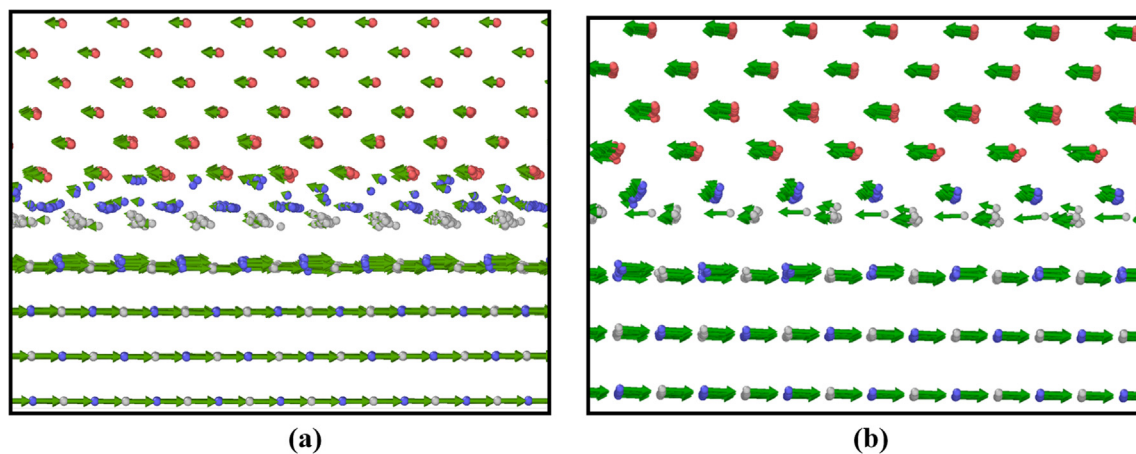
Overall, the maximum shear stress was shown to be significantly higher for Cr/TiN than for Ti/TiN and Cu/TiN as calculated in the previous work by the authors [62]. This is consistent with experimental results comparing the shear strength of Cr, Cu, and Ti in contact with CrN, which showed the highest shear strength for Cr [23]. Furthermore, Cr performed much better than Ti and Mo in wear and friction tests with TiC ceramic [104] due to its higher hardness and better adhesion.

Fig. 9 shows a plot of the magnitude of the relative displacement between layers as a function of the number of stress steps as mentioned in Section 2.3.3 for the coherent structure, and configurations with the MDN at the M = 1 and M = 5 layers. The plots for the other configurations studied are given in the Supplementary information (Fig. S2). Each stress step is scaled with respect to the step at which the shear failure occurs (where the shear force drops dramatically) to better compare among the different configurations. A unit value of this scaled stress step represents the initiation of fracture in all cases. It can be observed that for all configurations, shear failure occurs between the first and second ceramic layers in comparison to the chemical interface. This is different than what was observed at the Ti/TiN and Cu/TiN interfaces [62]. The likely reason for this is due to the different interfacial configuration of TiN at the Cr/TiN interface, in which the TiN (0 0 1) surface is in contact with Cr, while the TiN(1 1 1) surface is in contact with both Cu and Ti. This is also consistent with the work of adhesion at the Cr (0 0 1)/TiN (0 0 1) interface, which is 3.69 J/m^2, higher than the value of 1.70 J/m^2, observed one layer into the ceramic. When the MDN is at the M = 5 layer, a weak displacement can be observed between the M = 4 and M = 5 layers that forms before fracture occurs. Additionally, for the coherent system, there is a small displacement between the chemical interface and the M = 1 layer. However, none of these are enough to cause shear failure. The more gradual displacement observed when the MDN is at the M = 1 layer as indicated in Fig. 9(b) hints towards a plastic deformation behavior for that configuration, which will be discussed later.

To better illustrate where shear failure occurs, snapshots showing atom positions and their displacements with respect to their equilibrium positions are shown in Fig. 10 for the coherent system and for the configuration with MDNs located at the M = 1 layer. The displacement arrow magnitudes are set to be consistent within each individual system, but not with respect to one another. It is clear that shear failure occurs in both cases one layer into the ceramic from the Cr/TiN interface, and that under shear, the nitrogen atoms in the top ceramic layer shift towards the Cr metal with respect to the Ti atoms. The shifting that occurs under shear destabilizes the interaction between the first two layers of the TiN phase, causing shear failure to occur. Moreover, this destabilization is present in all MDN patterns studied in this work, being prevalent

Fig. 9. Plot of the difference in displacement (D) per layer per stress step for (a) coherent (b) MDN at M = 1 and (c) M = 5 layer.
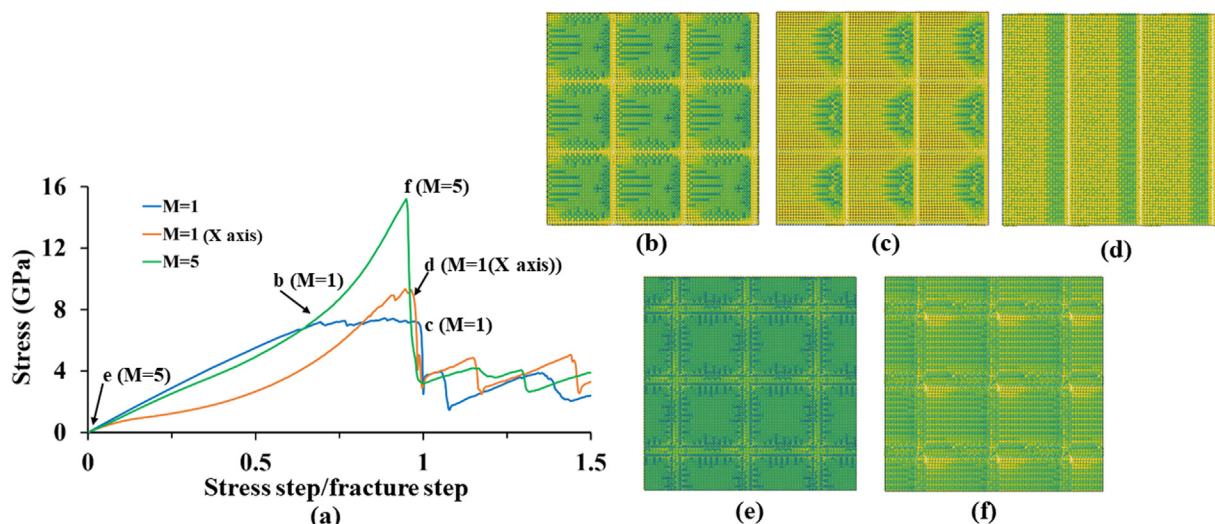

Fig. 10. Snapshots of the displacement of atoms immediately after shear failure (a) for coherent system and (b) for with MDNs at the M = 1 layer. Red atoms represent Cr, blue atoms N, and white atoms Ti. (For interpretation of the references to color in this figure legend, the reader is referred to the web version of this article.)

enough to overcome weaker interactions between Cr layers caused by the presence of these MDNs.

Fig. 11(a) shows the shear stress vs the stress step relative to shear failure for the Cr/TiN system with MDNs present at the M = 1 and M = 5 layers. The snapshots in Fig. 11(b-d) correspond to the letters in Fig. 11(a), all showing the M = 1 layer and all ceramic atoms. Atoms in the snapshots are color coded with respect to their CSP. For the system with MDNs at M = 1 along both X and Y

Fig. 11. (a) The plot of stress against the stress step scaled by the fracture step. (b-f) Snapshots of different configurations in the shear calculations as shown in the stress plot with letters on the stress plot corresponding to the snapshot letters in parenthesis.

axes, the elastic deformation was observed up to point **b** in the plot. Further shear loading resulted in a plastic deformation region for the metal/ceramic system leading to point **c**, as can be observed from the flattening of the stress curve in Fig. 11(a). In the corresponding snapshots, it can be observed that the nodes present in the minimum energy structure (see Fig. 5(a)) start to expand and move at point **b** as shown in Fig. 11(b). During the plastic deformation, the size of the locally disordered region expands until it propagates through the entire system when it reaches point **c** as shown in Fig. 11(c). When the MDN is only present in one direction, no specific nodes are present like they are when MDNs are present in the X and Y directions, and the yielding flows from the dislocation lines evenly as can be observed in Fig. 11(d). The consequence is a sharper peak in stress before shear failure, as can be observed near point **d**.

As described previously, when the MDNs are present at M = 5, the yielding does not occur at that layer to a significant amount, but near the chemical interface. Fig. 11(e) shows the equilibrium structure for the system with MDNs at M = 5, but unlike Fig. 5(c), the top layer shown is the M = 1 layer, which is closer to where shear failure occurs. It is apparent that the disorder induced by the MDN propagates to the interfacial region to a modest degree. Shown at point **f** in Fig. 11(a), a very sharp peak is present at shear failure with no plastic behavior. Fig. 11(f), which corresponds with this point, shows only a small amount disorder, which encompasses atoms close to the positions of the MDN in the M = 5 layer (four layers above what is shown). In general, MDNs in the M = 5 layer appears to have a modest impact on the structure at the interface, which lowers its shear strength in comparison with the coherent interface by around 4 GPa as shown in Fig. 8.

4. Conclusion

A new MEAM interatomic potential was developed to study Cr/TiN stability and shear strength. The new potential expanded upon a previously developed TiN model to parameterize new interactions for Cr, CrTi, CrN, and CrTiN. The potential was fit to experimental and density function theory derived thermodynamic, mechanical, and interfacial properties. In particular, the focus was on reproducing the GSFE for Cr/TiN interfacial systems since they were found to be important for describing the formation and stability of MDNs. Using the new MEAM model, large scale molecular dynamics simulations were used to determine the impact of MDN position on the stability and resistance to shear for the Cr/TiN interface. The main finding from the simulations was to show that Cr has the highest interfacial shear strength with TiN of the systems studied, which was linked to the fact that it had the highest GSFE barriers. Higher GSFE barriers were further linked to decreases in dislocation core widths. This showed the ability of properties calculated with relatively small *ab initio* calculations to be linked with macroscopic shear strength calculated with large scale simulations. Moreover, this leads to a new potential paradigm, in which results from small scale *ab initio* calculations can be used to design stronger interfaces with a reasonable degree of confidence.

For the Cr/TiN interface specifically, when the MDN was located adjacent to the chemical interface, it had the largest dislocation cores and the lowest interfacial energy. The larger dislocation nodes led to lower shear strength, and for this particular system, a significant plastic deformation region was present. As the MDN was moved farther away from the Cr/TiN interface, the interfacial core width decreased, the interfacial energy increased, and the shear strength increased. For all systems studied, shear failure occurred in the ceramic phase, between the first and second TiN layers form the Cr/TiN interface.

Declaration of Competing Interest

The authors declare that they have no known competing financial interests or personal relationships that could have appeared to influence the work reported in this paper.

Data Availability

The raw data required to reproduce these findings are available to download from https://drive.google.com/drive/folders/1JlmTo-TIuzY2VfnsmM2_9BtOn3IL61uZf?usp=sharing.

References

[1] N. Li, X.-Y. Liu, Review: mechanical behavior of metal/ceramic interfaces in nanolayered composites—experiments and modeling, J. Mater. Sci. 53 (2017) 5562–5583, https://doi.org/10.1007/s10853-017-1767-1.

[2] S.B. Sinnott, E.C. Dickey, Ceramic/metal interface structures and their relationship to atomic- and meso-scale properties, Mater. Sci. Eng.: R: Reports. 43 (2003) 1–59, https://doi.org/10.1016/j.mser.2003.09.001.

[3] N.P. Padture, Thermal barrier coatings for gas-turbine engine applications, Science 296 (2002) 280–284, https://doi.org/10.1126/science.1068609.

[4] A. Leyland, A. Matthews, On the significance of the H/E ratio in wear control: a nanocomposite coating approach to optimised tribological behaviour, Wear 246 (2000) 1–11, https://doi.org/10.1016/s0043-1648(00)00488-9.

[5] H. Bian, X. Song, S. Hu, Y. Lei, Y. Jiao, S. Duan, J. Feng, W. Long, Microstructure evolution and mechanical properties of titanium/alumina brazed joints for medical implants, Metals 9 (2019) 644, https://doi.org/10.3390/met9060644.

[6] M.C. Halbig, M.H. Jaskowiak, J.D. Kiser, D. Zhu, Evaluation of ceramic matrix composite technology for aircraft turbine engine applications, in: 51st AIAA Aerospace Sciences Meeting Including the New Horizons Forum and Aerospace Exposition 2013, 2013. 10.2514/6.2013-539.

[7] H.C. Lee, K. Kim, S.Y. Han, S.K. Choi, E. Lee, M. Jo, M.S. Yoo, K. Cho, Highly conductive flexible metal-ceramic nanolaminate electrode for high-performance soft electronics, ACS Appl. Mater. Interfaces 11 (2) (2019) 2211–2217, https://doi.org/10.1021/acsami.8b1482110.1021/acsami.8b14821.s001.

[8] D.A. Chance, D.L. Wilcox, Metal-ceramic constraints for multilayer electronic packages, Proc. IEEE 59 (10) (1971) 1455–1462, https://doi.org/10.1109/PROC.1971.8454.

[9] K.K. Chawla, Composite Materials, Springer New York, New York, NY, 1987. 10.1007/978-1-4757-3912-1.

[10] A.G. Evans, D.R. Mumm, J.W. Hutchinson, G.H. Meier, F.S. Pettit, Mechanisms controlling the durability of thermal barrier coatings, Prog. Mater Sci. 46 (5) (2001) 505–553, https://doi.org/10.1016/S0079-6425(00)00020-7.

[11] Y.L. Su, S.H. Yao, Z.L. Leu, C.S. Wei, C.T. Wu, Comparison of tribological behavior of three films—TiN, TiCN and CrN—grown by physical vapor deposition, Wear 213 (1-2) (1997) 165–174, https://doi.org/10.1016/S0043-1648(97)00182-8.

[12] I.A. Abrikosov, A. Knutsson, B. Alling, F. Tasnádi, H. Lind, L. Hultman, M. Odén, Phase Stability and Elasticity of TiAlN, Materials (Basel, Switzerland). 4 (2011) 1599–1618, https://doi.org/10.3390/ma4091599.

[13] S. Ding, X. Wang, A systematic study on the MEAM interatomic potentials of the transition metal nitrides TMNs (TM=Ti, V, Cr, Fe) binary systems, J. Alloy. Compd. 805 (2019) 1081–1089, https://doi.org/10.1016/j.jallcom.2019.07.114.

[14] J. Horník, S. Krum, D. Tondl, M. Puchnin, P. Sachr, L. Cvrček, Multilayer coatings Ti/TiN, Cr/CrN AND W/WN deposited by magnetron sputtering for improvement of adhesion to base materials, Acta Polytechnica. 55 (2015) 388–392. 10.14311/AP.2015.55.0388.

[15] I. Kim, F. Khatkhatay, L. Jiao, G. Swadener, J.I. Cole, J. Gan, H. Wang, TiN-based coatings on fuel cladding tubes for advanced nuclear reactors, J. Nucl. Mater. 429 (1-3) (2012) 143–148, https://doi.org/10.1016/j.jnucmat.2012.05.001.

[16] F. Khatkhatay, L. Jiao, J. Jian, W. Zhang, Z. Jiao, J. Gan, H. Zhang, X. Zhang, H. Wang, Superior corrosion resistance properties of TiN-based coatings on Zircaloy tubes in supercritical water, J. Nucl. Mater. 451 (1-3) (2014) 346–351, https://doi.org/10.1016/j.jnucmat.2014.04.010.

[17] P. Panjan, B. Navinšek, A. Cvelbar, A. Zalar, I. Milošev, Oxidation of TiN, ZrN, TiZrN, CrN, TiCrN and TiN/CrN multilayer hard coatings reactively sputtered at low temperature, Thin Solid Films 281–282 (1996) 298–301, https://doi.org/10.1016/0040-6090(96)08663-4.

[18] W.J. Meng, S. Shao, Experimentation and Modeling of Mechanical Integrity and Instability at Metal/Ceramic Interfaces, in: Handbook of Nonlocal Continuum Mechanics for Materials and Structures, Springer International Publishing, Cham, 2019. 10.1007/978-3-319-58729-5_50.

[19] F. Spaepen, Interfaces and stresses in thin films, Acta Mater. 48 (1) (2000) 31–42, https://doi.org/10.1016/S1359-6454(99)00286-4.

[20] G. Yang, Y. Liu, Z. Hang, N. Xi, H. Fu, H. Chen, Adhesion at cerium doped metal-ceramic α-Fe/WC interface: A first-principles calculation, J. Rare Earths 37 (7) (2019) 773–780, https://doi.org/10.1016/j.jre.2018.11.009.

[21] X. Guo, Y. Zhang, Y.-G. Jung, L. Li, J. Knapp, J. Zhang, Ideal tensile strength and shear strength of ZrO2(111)/Ni(111) ceramic-metal Interface: A first principle study, Mater. Des. 112 (2016) 254–262, https://doi.org/10.1016/j.matdes.2016.09.073.

[22] X. Zhou, W. Bu, S. Song, F. Sansoz, X. Huang, Multiscale modeling of interfacial mechanical behaviours in SiC/Mg nanocomposites, Mater. Des. 182 (2019), https://doi.org/10.1016/J.MATDES.2019.108093 108093.

[23] Y. Mu, X. Zhang, J. Hutchinson, W. Meng, Measuring critical stress for shear failure of interfacial regions in coating/interlayer/substrate systems through a micro-pillar testing protocol, J. Mater. Res. 32 (2017) 1–11, https://doi.org/10.1557/jmr.2016.516.

[24] K.e. Chen, Y. Mu, W.J. Meng, A new experimental approach for evaluating the mechanical integrity of interfaces between hard coatings and substrates, MRS Commun. 4 (1) (2014) 19–23, https://doi.org/10.1557/mrc.2014.3.

[25] M. Gsellmann, T. Klünsner, C. Mitterer, M. Krobath, M. Wurmshuber, H. Leitner, W. Ecker, S. Marsoner, V. Maier-Kiener, D. Kiener, G. Ressel, Strength ranking for interfaces between a TiN hard coating and microstructural constituents of high speed steel determined by micromechanical testing, Mater. Des. 204 (2021), https://doi.org/10.1016/J.MATDES.2021.109690 109690.

[26] W. Ecker, J. Keckes, M. Krobath, J. Zalesak, R. Daniel, M. Rosenthal, J. Todt, Nanoscale evolution of stress concentrations and crack morphology in multilayered CrN coating during indentation: Experiment and simulation, Mater. Des. 188 (2020) 108478, https://doi.org/10.1016/j.matdes.2020.108478.

[27] N. Li, H. Wang, A. Misra, J. Wang, In situ Nanoindentation Study of Plastic Co-deformation in Al-TiN Nanocomposites, Scientific Reports 2014 4:1. 4 (2014) 1–6. 10.1038/srep06633.

[28] C. Mayer, N. Li, N. Mara, N. Chawla, Micromechanical and in situ shear testing of Al–SiC nanolaminate composites in a transmission electron microscope (TEM), Mater. Sci. Eng., A 621 (2015) 229–235, https://doi.org/10.1016/J.MSEA.2014.10.055.

[29] P. Wieciński, J. Smolik, H. Garbacz, K.J. Kurzydłowski, Failure and deformation mechanisms during indentation in nanostructured Cr/CrN multilayer coatings, Surf. Coat. Technol. 240 (2014) 23–31, https://doi.org/10.1016/j.surfcoat.2013.12.006.

[30] D. Li, S. Guruvenket, S. Hassani, E. Bousser, M. Azzi, J.A. Szpunar, J.E. Klemberg-Sapieha, Effect of Cr interlayer on the adhesion and corrosion enhancement of nanocomposite TiN-based coatings deposited on stainless steel 410, Thin Solid Films 519 (10) (2011) 3128–3134, https://doi.org/10.1016/j.tsf.2010.12.020.

[31] W. Guan, H. Zhu, W. Zhu, Z. Chen, J. Liu, X. Shi, X. Wang, Effects of the different interlayer deposition processes on the microstructure of Cr/tiN coating, Mater. Res. Express 6 (2019), https://doi.org/10.1088/2053-1591/ab67f4 126444.

[32] N.D. Nam, M.J. Kim, D.S. Jo, J.G. Kim, D.H. Yoon, Corrosion protection of Ti/TiN, Cr/TiN, Ti/CrN, and Cr/CrN multi-coatings in simulated proton exchange membrane fuel cell environment, Thin Solid Films 545 (2013) 380–384, https://doi.org/10.1016/j.tsf.2013.07.056.

[33] S. Han, J.H. Lin, S.H. Tsai, S.C. Chung, D.Y. Wang, F.H. Lu, H.C. Shih, Corrosion and tribological studies of chromium nitride coated on steel with an interlayer of electroplated chromium, Surf. Coat. Technol. 133–134 (2000) 460–465, https://doi.org/10.1016/S0257-8972(00)00979-8.

[34] R. Bayón, A. Igartua, X. Fernández, R. Martínez, R.J. Rodríguez, J.A. García, A. de Frutos, M.A. Arenas, J. de Damborenea, Corrosion-wear behaviour of PVD Cr/CrN multilayer coatings for gear applications, Tribol. Int. 42 (4) (2009) 591–599, https://doi.org/10.1016/j.triboint.2008.06.015.

[35] T. Polcar, R. Martinez, T. Vítů, L. Kopecký, R. Rodriguez, A. Cavaleiro, High temperature tribology of CrN and multilayered Cr/CrN coatings, Surf. Coat. Technol. 203 (20-21) (2009) 3254–3259, https://doi.org/10.1016/j.surfcoat.2009.04.005.

[36] J.-H. Park, H.-G. Kim, J.-Y. Park, Y.-I. Jung, D.-J. Park, Y.-H. Koo, High temperature steam-oxidation behavior of arc ion plated Cr coatings for accident tolerant fuel claddings, Surf. Coat. Technol. 280 (2015) 256–259, https://doi.org/10.1016/j.surfcoat.2015.09.022.

[37] K. Yang, B. Liao, H. Zhu, W. Zhu, H. He, Y. Liu, H. Li, X. Wang, Influence of the Cr interlayer on the microstructure of sputtered TiN coatings deposited on zirconium alloy, Mater. Res. Express 6 (2019), https://doi.org/10.1088/2053-1591/aaf041 026420.

[38] A.G. Evans, J.W. Hutchinson, Y. Wei, Interface adhesion: effects of plasticity and segregation, Acta Mater. 47 (1999) 4093–4113, https://doi.org/10.1016/s1359-6454(99)00269-4.

[39] W. Zhang, J.R. Smith, Nonstoichiometric Interfaces andAl2O3Adhesion with Al and Ag, Phys. Rev. Lett. 85 (2000) 3225–3228, https://doi.org/10.1103/physrevlett.85.3225.

[40] D.J. Siegel, L.G. Hector, J.B. Adams, First-principles study of metal–carbide/nitride adhesion: Al/VC vs, Al/VN, Acta Materialia. 50 (3) (2002) 619–631, https://doi.org/10.1016/S1359-6454(01)00361-5.

[41] D. Bhattacharyya, X.-Y. Liu, A. Genc, H.L. Fraser, R.G. Hoagland, A. Misra, Heterotwin formation during growth of nanolayered Al-TiN composites, Appl. Phys. Lett. 96 (2010), https://doi.org/10.1063/1.3330889 093113.

[42] N. Li, S.K. Yadav, J. Wang, X.-Y. Liu, A. Misra, Growth and Stress-induced Transformation of Zinc blende AlN Layers in Al-AlN-TiN Multilayers, Sci. Rep. 5 (2015) 18554, https://doi.org/10.1038/srep18554.

[43] Z. Li, S. Yadav, Y. Chen, N. Li, X.-Y. Liu, J. Wang, S. Zhang, J.K. Baldwin, A. Misra, N. Mara, Mechanically controlling the reversible phase transformation from zinc blende to wurtzite in AlN, Mater. Res. Lett. 5 (6) (2017) 426–432, https://doi.org/10.1080/21663831.2017.1303793.

[44] H.Z. Zhang, L.M. Liu, S.Q. Wang, First-principles study of the tensile and fracture of the Al/TiN interface, Comput. Mater. Sci. 38 (4) (2007) 800–806, https://doi.org/10.1016/j.commatsci.2006.05.017.

[45] S.K. Yadav, R. Ramprasad, A. Misra, X.-Y. Liu, First-principles study of shear behavior of Al, TiN, and coherent Al/TiN interfaces, J. Appl. Phys. 111 (2012), https://doi.org/10.1063/1.3703663 083505.

[46] A.S. Mohammad Miraz, S. Sun, S. Shao, W.J. Meng, B.R. Ramachandran, C.D. Wick, Computational study of metal/ceramic interfacial adhesion and barriers to shear displacement, Comput. Mater. Sci. 168 (2019) 104–115, https://doi.org/10.1016/j.commatsci.2019.06.006.

[47] B.-J. Lee, M.I. Baskes, Second nearest-neighbor modified embedded-atom-method potential, Phys. Rev. B. 62 (13) (2000) 8564–8567, https://doi.org/10.1103/PhysRevB.62.8564.

[48] M.I. Baskes, Application of the embedded-atom method to covalent materials: A semiempirical potential for silicon, Phys. Rev. Lett. 59 (23) (1987) 2666–2669, https://doi.org/10.1103/PhysRevLett.59.2666.

[49] M.S. Daw, M.I. Baskes, Embedded-atom method: Derivation and application to impurities, surfaces, and other defects in metals, Phys. Rev. B. 29 (1984) 6443–6453, https://doi.org/10.1103/physrevb.29.6443.

[50] M.I. Baskes, R.A. Johnson, Modified embedded atom potentials for HCP metals, Modell. Simul. Mater. Sci. Eng. 2 (1) (1994) 147–163, https://doi.org/10.1088/0965-0393/2/1/011.

[51] M.I. Baskes, J.S. Nelson, A.F. Wright, Semiempirical modified embedded-atom potentials for silicon and germanium, Phys. Rev. B. 40 (9) (1989) 6085–6100, https://doi.org/10.1103/PhysRevB.40.6085.

[52] M.S. Daw, S.M. Foiles, M.I. Baskes, The embedded-atom method: a review of theory and applications, Mater. Sci. Reports 9 (1993) 251–310, https://doi.org/10.1016/0920-2307(93)90001-u.

[53] B.-J. Lee, W.-S. Ko, H.-K. Kim, E.-H. Kim, The modified embedded-atom method interatomic potentials and recent progress in atomistic simulations, Calphad. 34 (4) (2010) 510–522, https://doi.org/10.1016/j.calphad.2010.10.007.

[54] X. Yuan, K. Takahashi, Y. Yin, T. Onzawa, Development of modified embedded atom method for a bcc metal: lithium, Modell. Simul. Mater. Sci. Eng. 11 (4) (2003) 447–456, https://doi.org/10.1088/0965-0393/11/4/303.

[55] S.M. Foiles, M.I. Baskes, M.S. Daw, Embedded-atom-method functions for the fcc metals Cu, Ag, Au, Ni, Pd, Pt, and their alloys, Phys. Rev. B. 33 (12) (1986) 7983–7991, https://doi.org/10.1103/PhysRevB.33.7983.

[56] J. Wang, B.J. Lee, Second-nearest-neighbor modified embedded-atom method interatomic potential for V-M (M = Cu, Mo, Ti) binary systems, Comput. Mater. Sci. 188 (2021), https://doi.org/10.1016/J.COMMATSCI.2020.110177 110177.

[57] B. Narayanan, K. Sasikumar, Z.-G. Mei, A. Kinaci, F.G. Sen, M.J. Davis, S.K. Gray, M.K.Y. Chan, S.K.R.S. Sankaranarayanan, Development of a Modified Embedded Atom Force Field for Zirconium Nitride Using Multi-Objective Evolutionary Optimization, J. Phys. Chem. C 120 (31) (2016) 17475–17483, https://doi.org/10.1021/acs.jpcc.6b0529610.1021/acs.jpcc.6b05296.s001.

[58] Y.-M. Kim, B.-J. Lee, Modified embedded-atom method interatomic potentials for the Ti–C and Ti–N binary systems, Acta Mater. 56 (14) (2008) 3481–3489, https://doi.org/10.1016/j.actamat.2008.03.027.

[59] I. Aslam, M.I. Baskes, D.E. Dickel, S. Adibi, B. Li, H. Rhee, M. Asle Zaeem, M.F. Horstemeyer, Thermodynamic and kinetic behavior of low-alloy steels: An atomic level study using an Fe-Mn-Si-C modified embedded atom method (MEAM) potential, Materialia. 8 (2019), https://doi.org/10.1016/j.mtla.2019.100473 100473.

[60] A.E. Gheribi, Molecular dynamics study of stable and undercooled liquid zirconium based on MEAM interatomic potential, Mater. Chem. Phys. 116 (2-3) (2009) 489–496, https://doi.org/10.1016/j.matchemphys.2009.04.020.

[61] M.G. Elkhateeb, Y.C. Shin, Molecular dynamics-based cohesive zone representation of Ti6Al4V/TiC composite interface, Mater. Des. 155 (2018) 161–169, https://doi.org/10.1016/J.MATDES.2018.05.054.

[62] A.S.M. Miraz, N. Dhariwal, W.J. Meng, B.R. Ramachandran, C.D. Wick, Development and application of interatomic potentials to study the stability and shear strength of Ti/TiN and Cu/TiN interfaces, Mater. Des. 196 (2020), https://doi.org/10.1016/j.matdes.2020.109123 109123.

[63] E.Y. Chen, R. Dingreville, C. Deo, Misfit dislocation networks in semi-coherent miscible phase boundaries: An example for U-Zr interfaces, Comput. Mater. Sci. 154 (2018) 194–203, https://doi.org/10.1016/j.commatsci.2018.07.065.

[64] D. Cheng, Z.J. Yan, L.i. Yan, Misfit dislocation network in Cu/Ni multilayers and its behaviors during scratching, Thin Solid Films 515 (7-8) (2007) 3698–3703, https://doi.org/10.1016/j.tsf.2006.10.001.

[65] S.K. Yadav, S. Shao, J. Wang, X.-Y. Liu, Structural modifications due to interface chemistry at metal-nitride interfaces, Sci. Rep. 5 (2015) 17380, https://doi.org/10.1038/srep17380.

[66] V. Bonu, M. Jeevitha, V. Praveen Kumar, H.C. Barshilia, Nanolayered multilayer Ti/TiN coatings: Role of bi-layer thickness and annealing on solid particle erosion behaviour at elevated temperature, Surf. Coat. Technol. 357 (2019) 204–211, https://doi.org/10.1016/j.surfcoat.2018.10.007.

[67] W. Yang, G. Ayoub, I. Salehinia, B. Mansoor, H. Zbib, The effect of layer thickness ratio on the plastic deformation mechanisms of nanoindented Ti/TiN nanolayered composite, Comput. Mater. Sci. 154 (2018) 488–498, https://doi.org/10.1016/j.commatsci.2018.08.021.

[68] M.I. Baskes, Determination of modified embedded atom method parameters for nickel, Mater. Chem. Phys. 50 (2) (1997) 152–158, https://doi.org/10.1016/S0254-0584(97)80252-0.

[69] J.H. Rose, J.R. Smith, F. Guinea, J. Ferrante, Universal features of the equation of state of metals, Phys. Rev. B. 29 (6) (1984) 2963–2969, https://doi.org/10.1103/PhysRevB.29.2963.

[70] B.-J. Lee, M.I. Baskes, H. Kim, Y. Koo Cho, Second nearest-neighbor modified embedded atom method potentials for bcc transition metals, Phys. Rev. B. 64 (2001), https://doi.org/10.1103/physrevb.64.184102.

[71] L.-Z. He, J. Zhu, L. Zhang, First-principles study of structural phase transition, electronic, elastic and thermodynamic properties of C15-type Laves phase TiCr2 under pressure, Phys. B 531 (2018) 79–84, https://doi.org/10.1016/j.physb.2017.11.051.

[72] Z.-S. Nong, J.-C. Zhu, H.-L. Yu, Z.-H. Lai, First principles calculation of intermetallic compounds in FeTiCoNiVCrMnCuAl system high entropy alloy, Trans. Nonferrous Metals Soc. China (English Edition). 22 (6) (2012) 1437–1444, https://doi.org/10.1016/S1003-6326(11)61338-1.

[73] S. Sun, B.R. Ramachandran, C.D. Wick, Solid, liquid, and interfacial properties of TiAl alloys: parameterization of a new modified embedded atom method model, J. Phys.: Condens. Matter 30 (2018), https://doi.org/10.1088/1361-648x/aaa52c 075002.

[74] G. Kresse, J. Furthmüller, Efficient iterative schemes for ab initio total-energy calculations using a plane-wave basis set, Physical Review B - Condensed Matter and Materials, Physics. 54 (16) (1996) 11169–11186, https://doi.org/10.1103/PhysRevB.54.11169.

[75] J.P. Perdew, K. Burke, M. Ernzerhof, Generalized Gradient Approximation Made Simple, Phys. Rev. Lett. 77 (18) (1996) 3865–3868, https://doi.org/10.1103/PhysRevLett.77.3865.

[76] J. Hafner, Ab-initiosimulations of materials using VASP: Density-functional theory and beyond, J. Comput. Chem. 29 (2008) 2044–2078, https://doi.org/10.1002/jcc.21057.

[77] G. Kresse, D. Joubert, From ultrasoft pseudopotentials to the projector augmented-wave method, Physical Review B - Condensed Matter and Materials, Physics. 59 (3) (1999) 1758–1775, https://doi.org/10.1103/PhysRevB.59.1758.

[78] H.J. Monkhorst, J.D. Pack, Special points for Brillouin-zone integrations, Phys. Rev. B. 13 (12) (1976) 5188–5192, https://doi.org/10.1103/PhysRevB.13.5188.

[79] A.S.M. Miraz, E. Williams, W.J. Meng, B.R. Ramachandran, C.D. Wick, Improvement of Ti/TiN interfacial shear strength by doping – A first principles density functional theory study, Appl. Surface Sci. 517 (2020) 146185. https://www.sciencedirect.com/science/article/pii/S0169433220309417.

[80] T. Hong, J.R. Smith, D.J. Srolovitz, Theory of metal–Ceramic adhesion, Acta Metall. Mater. 43 (7) (1995) 2721–2730, https://doi.org/10.1016/0956-7151(94)00457-S.

[81] S. Plimpton, Fast parallel algorithms for short-range molecular dynamics, J. Comput. Phys. 117 (1) (1995) 1–19, https://doi.org/10.1006/jcph.1995.1039.

[82] W.G. Hoover, Canonical dynamics: Equilibrium phase-space distributions, Phys. Rev. A 31 (1985) 1695–1697, https://doi.org/10.1103/PhysRevA.31.1695.

[83] S. Nosé, A unified formulation of the constant temperature molecular dynamics methods, J. Chem. Phys. 81 (1) (1984) 511–519, https://doi.org/10.1063/1.447334.

[84] I. Salehinia, S. Shao, J. Wang, H.M. Zbib, Interface structure and the inception of plasticity in Nb/NbC nanolayered composites, Acta Mater. 86 (2015) 331–340, https://doi.org/10.1016/j.actamat.2014.12.026.

[85] X. Zhang, B. Zhang, Y. Mu, S. Shao, C.D. Wick, B.R.R. Ramachandran, W.J. Meng, Mechanical failure of metal/ceramic interfacial regions under shear loading, Acta Mater. 138 (2017) 224–236, https://doi.org/10.1016/j.actamat.2017.07.053.

[86] P.K. Misra, Physics of Condensed Matter, Academic Press, 2010. 10.1016/C2010-0-65289-8.

[87] C. Kittel, Introduction to Solid State Physics, 8th ed., John Wiley & Sons Inc., 2004. 10.1119/1.1974177.

[88] W.-M. Choi, Y. Kim, D. Seol, B.-J. Lee, Modified embedded-atom method interatomic potentials for the Co-Cr, Co-Fe, Co-Mn, Cr-Mn and Mn-Ni binary systems, Comput. Mater. Sci. 130 (2017) 121–129, https://doi.org/10.1016/j.commatsci.2017.01.002.

[89] H. Schultz, Atomic Defects in Metals. Cr, in: H. Ullmaier (Ed.), Atomic Defects in Metals, Springer-Verlag, 1991. 10.1007/B37800.

[90] W.R. Tyson, W.A. Miller, Surface free energies of solid metals: Estimation from liquid surface tension measurements, Surf. Sci. 62 (1977) 267–276, https://doi.org/10.1016/0039-6028(77)90442-3.

[91] D.I. Bolef, J. de Klerk, Anomalies in the Elastic Constants and Thermal Expansion of Chromium Single Crystals, Phys. Rev. 129 (3) (1963) 1063–1067, https://doi.org/10.1103/PhysRev.129.1063.

[92] W.M. Haynes, CRC Handbook of Chemistry and Physics, 92nd ed., Boca Raton, FL, 2012. https://www.amazon.com/CRC-Handbook-Chemistry-Physics-92nd/dp/1439855110.

[93] F. Kong, R.C. Longo, C. Liang, Y. Nie, Y. Zheng, C. Zhang, K. Cho, Charge-transfer modified embedded atom method dynamic charge potential for Li–Co–O system, J. Phys.: Condens. Matter 29 (47) (2017) 475903, https://doi.org/10.1088/1361-648X/aa9420.

[94] F. Kong, R.C. Longo, C. Liang, D.H. Yeon, Y. Zheng, J.H. Park, S.G. Doo, K. Cho, CT-MEAM interatomic potential of the Li-Ni-O ternary system for Li-ion battery cathode materials, Comput. Mater. Sci. 127 (2017) 128–135, https://doi.org/10.1016/J.COMMATSCI.2016.10.030.

[95] C.-L. Kuo, P. Clancy, Development of atomistic MEAM potentials for the silicon-oxygen-gold ternary system, Modell. Simul. Mater. Sci. Eng. 13 (8) (2005) 1309–1329, https://doi.org/10.1088/0965-0393/13/8/008.

[96] K.J. Martinschitz, R. Daniel, C. Mitterer, J. Keckes, Elastic constants of fibre-textured thin films determined by X-ray diffraction, J. Appl. Crystallogr. 42 (3) (2009) 416–428, https://doi.org/10.1107/S0021889809011807.

[97] A. Pathak, A.K. Singh, Transition Metal Nitrides: A First Principles Study, High Temp. Mater. Processes (London) 35 (2016) 389–398, https://doi.org/10.1515/htmp-2014-0169.

[98] V. Antonov, I. Iordanova, First principles study of crystallographic structure and elastic properties of chromium nitride, in: AIP Conference Proceedings, American Institute of PhysicsAIP, 2010: pp. 1149–1154. 10.1063/1.3322328.

[99] A. Hunter, R.F. Zhang, I.J. Beyerlein, The core structure of dislocations and their relationship to the material γ-surface, J. Appl. Phys. 115 (2014), https://doi.org/10.1063/1.4870462 134314.

[100] S. Shao, J. Wang, A. Misra, Energy minimization mechanisms of semi-coherent interfaces, J. Appl. Phys. 116 (2014), https://doi.org/10.1063/1.4889927 023508.

[101] S. Shao, J. Wang, Relaxation mechanisms, structure and properties of semi-coherent interfaces, Metals 5 (2015) 1887–1901, https://doi.org/10.3390/met5041887.

[102] A. Stukowski, Structure identification methods for atomistic simulations of crystalline materials, Modell. Simul. Mater. Sci. Eng. 20 (4) (2012) 045021, https://doi.org/10.1088/0965-0393/20/4/045021.

[103] C.L. Kelchner, S.J. Plimpton, J.C. Hamilton, Dislocation nucleation and defect structure during surface indentation, Phys. Rev. B. 58 (17) (1998) 11085–11088, https://doi.org/10.1103/PhysRevB.58.11085.

[104] J. Tang, L.i. Feng, J.S. Zabinski, The effects of metal interlayer insertion on the friction, wear and adhesion of TiC coatings, Surf. Coat. Technol. 99 (3) (1998) 242–247, https://doi.org/10.1016/S0257-8972(97)00570-7.